# Power stabilization of a terahertz-frequency quantum-cascade laser using a photonic-integrated modulator

**S. S. KONDAWAR,**[1,*] **N. K. NORTH,**[1] **Y. HAN,**[1] **D. PARDO,**[2] **N. BREWSTER,**[2] **M. D. HORBURY,**[1] **M. SALIH,**[1] **L. LI,**[1] **P. DEAN,**[1] **J. R. FREEMAN,**[1] **B. N. ELLISON,**[2] **I. KUNDU,**[1,3] **AND A. VALAVANIS**[1]

[1] *School of Electronic and Electrical Engineering, The University of Leeds, Leeds LS2 9JT, UK*
[2] *UKRI–STFC Rutherford Appleton Laboratory, Harwell Oxford, Didcot OX11 0QX, UK*
[3] *Currently with Optalysys Ltd., 8 Flemming Court, Wakefield WF10 5HW, UK*
*\*s.kondawar@leeds.ac.uk*

**Abstract:** We demonstrate a technique to stabilize the emission from a 3.4-THz quantum-cascade laser against power drifts, using a recently developed photonic integrated circuit (PIC) structure formed by coupling a racetrack resonator with a ridge waveguide. This structure enables a dynamic power-control range of ±15% and locking over >600 s using a proportional–integral control loop. The resonator yields a 50% weaker perturbation to the laser emission frequency when compared with direct laser modulation, and hence offers the prospect of simultaneous, quasi-independent control of power and frequency. Progress towards integrating the PIC with a precision micromachined rectangular metallic waveguide module has also been demonstrated, with power modulation of the principal laser emission line being observed during pulsed operation.

## 1. Introduction

Terahertz-frequency quantum cascade lasers (THz QCLs) are compact semiconductor sources of narrowband radiation within the ~2–5-THz band [1]. Owing to their compact size, low power consumption, and high continuous-wave output power, they have potential for use in a wide range of applications including security imaging, biomedical sensing, communications, and space-based research [2]. However, their high sensitivity to temperature [3] and optical feedback [4] results in the output power delivered to a given application system being inherently unstable. Variations in atmospheric humidity [5], thermal drift and mechanical vibrations (e.g., from cryocoolers) [6] also introduce fluctuations in the transmitted THz power, causing significant drifts in system performance. It is, therefore, desirable to provide active power stabilization.

Several QCL power stabilization techniques have been developed, including the use of a swing-arm voice coil actuator as a variable beam-block [6], a graphene-loaded split-ring-resonator array as an external amplitude modulator [7], and illumination with an external diode laser to perturb QCL emission [8]. All these techniques, however, rely on external optical elements, which increase system size and complexity, and may limit their applicability to certain application environments. For example, mass, volume, and power are critical parameters in satellite system design, along with potentially slow thermal stabilization from low powered cryocoolers. It has also been demonstrated experimentally that frequency noise and amplitude noise are anti-correlated in QCLs [6]. This implies that direct modulation of QCLs via their drive current can only stabilize one parameter at the expense of destabilizing the other. As such, it is desirable to develop an indirect power modulation scheme, which is independent from the QCL bias.

In this work, we present the power modulation and stabilization of THz QCLs using a recently demonstrated photonic integrated circuit (PIC) technique. Several THz-PIC approaches have been demonstrated including integration of THz QCLs with mixers [9], graphene modulators for surface emission [10], Vernier tuning [11], and frequency-selective coupled cavities [12]. Until recently, however, there has been a lack of modulator approaches suitable for planar integrated systems, owing to the long wavelengths ($\lambda \sim 60 - 150$ μm) emitted by THz QCLs. For example, Mach–Zehnder interferometers would require an impractically long cavity to achieve a useful modulation depth through electro-optic phase shifting.

Here, we exploit a planar PIC modulator device formed by coupling a racetrack resonator (RTR) with a QCL ridge waveguide using a co-directional coupler [13]. This coupled-RTR structure is used extensively for filters and modulators in telecom lasers and silicon photonics [14]. By varying the electrical bias on the RTR, the stopband frequencies of the RTR can be brought in and out of resonance with the optical modes of the QCL ridge. The net THz gain in the device can, therefore, be controlled, resulting in THz power modulation. The power-locking bandwidth is also potentially very high, owing to the sub-nanosecond gain dynamics in coupled cavity THz QCLs [15]. This approach has been shown previously to enable ~25% modulation of the THz QCL power, without significant perturbation to the laser frequency.

We demonstrate that the QCL-RTR system can be used to realize THz power stabilization using a proportional–integral control system, over a > 600-s timescale. In the following sections, we discuss the structure and performance of the modulator photonic circuit, and its operation within a power stabilization loop. We also demonstrate the integration of the PIC into an external precision-micromachined waveguide module.

## 2.    Device design and characterization

The THz-PIC systems developed for this work were close reproductions of those described in detail previously [13], and are summarized as follows. The PIC was based on a GaAs/AlGaAs ~3.4-THz QCL heterostructure [16]. A 4-mm-long by 48-μm-wide QCL Au–Au plasmonic ridge waveguide was fabricated using a maskless direct-write photolithography process, with the ridge optically coupled along its length to an RTR, as shown in Fig. 1. As in Ref. [13], the RTR consisted of four 565-μm-long straight sections, linked into a closed loop using curved segments with 893.52-μm arc radius to form a total RTR length of $L_{RTR}$ = 9.144 mm. The QCL ridge was positioned parallel to one of the straight sections of the RTR, with an airgap providing electrical isolation between the two optically coupled devices. A 2.5-μm-wide gap was used (c.f. 3-μm in Ref. [13]), although in practice this is expected only to yield a minor increase in the optical coupling at the frequency of the QCL, and as such all other system dimensions are left unchanged. Two 88-μm-wide by 500-μm-long sections were included in each device, as shown by ellipses in Fig. 1, to facilitate electrical wire bonding. The top metallic contacts on the QCL and RTR were 8-μm narrower than the semiconductor region, providing a lossy region at each edge to suppress higher-order transverse optical modes.

A detailed discussion of the optical mode structure, and tuning effects in the QCL and RTR cavities is given in previous work [13] and is summarized as follows. The QCL acts as a Fabry–Pérot cavity, supporting longitudinal modes separated by a free-spectral range, $FSR_{QCL} \approx c/(2n_g L)$, where $c$ is the speed of light, and $n_g \approx 3.7$ is the group index of the material. As the THz field within the QCL propagates from one end of the device to the other, part of the radiation is coupled into the resonator section. The RTR acts as a notch filter, with a comb of stop bands with a free-spectral range $FSR_{RTR} = c/(n_g L_{RTR}) \approx 9$ GHz. At zero bias, the FSR of the RTR was chosen to be slightly smaller than that of the QCL, such that the RTR stopband frequencies are out of alignment with the emission peaks of the QCL. Although the application of an electrical bias to the RTR causes a reduction in the intersubband losses, there is a corresponding shift in $n_g$ (via the Kramers–Krönig relationship), and hence an adjustment to
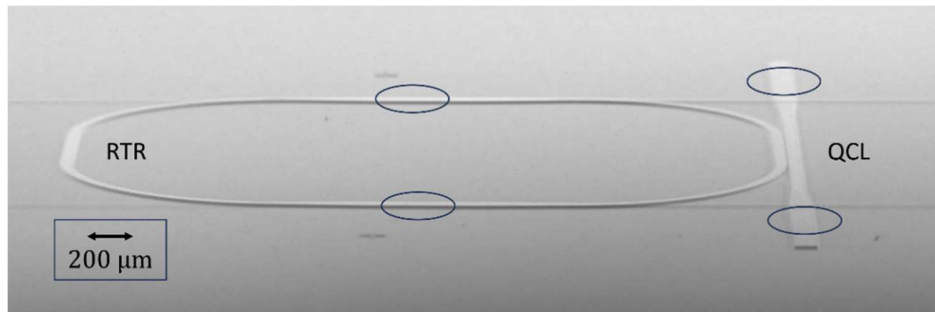
**Fig. 1.** Electron micrograph of photonic-integrated circuit, showing the racetrack resonator on the left, optically coupled to the QCL ridge on the right. Wire-bonding pads are indicated by elliptical markers.

the stopband frequencies. As the RTR shifts towards resonance with the QCL, the THz field coupling between the RTR and QCL increases. Since the RTR is operated at currents below its transparency point, it remains lossy, and a reduction in output power is obtained. Indeed, this stopband alignment effect has previously been verified experimentally through observation of the emission spectra as the RTR bias is brought towards transparency (Figs. 4 and 5 of Ref. [13]).

The QCL-PIC was mounted inside a Janis ST-100 helium cryostat at 40 K and the QCL ridge was driven electrically in continuous-wave (cw) mode using a benchtop dc power supply. The RTR was initially left unbiased, such that it acted as a lossy, passive resonator. The laser emission was modulated at 165 Hz using an optical chopper and coupled into a helium cooled QMC QSIB/3 silicon bolometric detector with a responsivity of ~15 V/mW and system noise of ~32 nV/$\sqrt{\text{Hz}}$. A Signal Recovery lock-in amplifier was used to demodulate and record the resulting detector signal. Figure 2(a) shows the detector signal and voltage of the QCL plotted as a function of the drive current, with the ring modulator switched off. Although the QCL operates up to a heatsink temperature of 63 K in cw mode, our subsequent power-locking investigation was performed at 40 K to provide a balance between output power, and cryostat temperature stability. At this temperature, the QCL lases at 0.5-A threshold current and has a peak emission power of ~80 μW at a drive current of 1.30 A. Discontinuities are seen in the measured THz power as a function of current, which correspond to the emission mode-hops shown later, in Fig. 3(a). The abrupt changes in detected power are likely to result from differences in atmospheric attenuation, and far-field spatial profile associated with each mode. In our subsequent measurements, we avoid these effects by biasing the QCL at its peak power.

An Arroyo 4302 laser driver was used to apply an independent bias to the RTR section, while the QCL ridge was maintained at its peak emission bias. The RTR was operated below 1-A drive current, such that it remained below its lasing threshold, and acted as a lossy cavity. Figure 2(b) shows that the output power of the QCL decreases as the RTR bias increases. The functional form of the power decrease is determined by the overlapping cavity resonances, which can be determined through semi-analytical solutions of Mason's gain formula [13]. However, a linear fit of the form $P_{\text{THz}} = P_0(1 - kI_{\text{RTR}})$, gives an adequate approximation when the QCL and RTR are approaching resonance, where $P_0$ is the unperturbed output power, and $k \approx 0.29$ A$^{-1}$ is a linear power-tuning coefficient. As such, this represents a ±15% dynamic range for subsequent power-locking, if the RTR is operated around a quiescent 0.5-A dc bias point. The electrical power consumption of the RTR element ranged from 0–5.4 W, which is comparable to that of the QCL ridge. We have previously shown [13], however, that the coupled-cavity has a much stronger effect on the QCL emission than the ~100 MHz/K [17] direct effect from Joule heating.
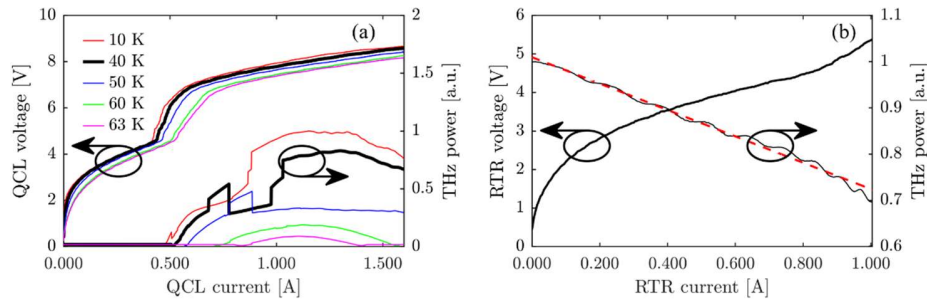
**Fig. 2.** Normalized THz detector signal, and terminal voltage for the QCL–RTR device. Results are shown for (a) QCL *I–V* characteristics, with the RTR unbiased, and results shown at a range of heatsink temperatures. The bold line denotes the characteristics at 40 K. (b) RTR *I–V* characteristics, with the QCL at a fixed current of 1.30 A and heatsink temperature of 40 K. The red dashed line shows a linear fit to the THz power as a function of RTR current.
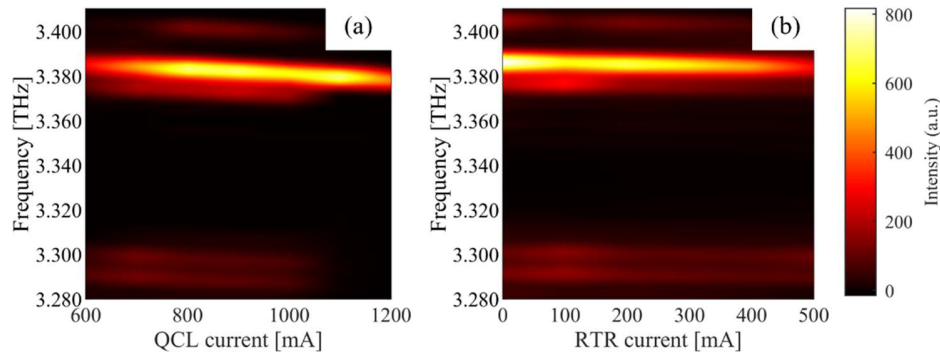


**Fig. 3.** Emission spectra of the QCL/modulator device obtained using an FTIR spectrometer. (a) at a range of QCL drive currents, with the modulator switched off, and (b) with the QCL at a fixed bias of 1.30 A and the ring-modulator driven at a range of currents.

Figure 3(a) shows the emission spectrum from one facet of the QCL at a range of drive currents, obtained using a Bruker IFS/66 Fourier Transform Infrared (FTIR) spectrometer. Radiation from the device is emitted within a principal mode around 3.38 THz, with several weaker modes present. By varying the drive current of the QCL, the frequency of the principal mode can be adjusted over a range of ~8 GHz, with a linear tuning coefficient, $\gamma_{QCL} = -12 \pm 2$ MHz/mA.

By contrast, Fig. 3(b) shows a ~50% weaker tuning coefficient, $\gamma_{RTR} = -6 \pm 2$ MHz/mA, as the modulator bias varies. This large difference in tuning is desirable for a power modulator, as the output power may be adjusted quasi-independently from the laser emission frequency.

## 3. Power locking

A power-locking loop was implemented as shown schematically in Fig. 4, to stabilize the QCL emission against slow, long-term power drifts. In this configuration, the demodulated detector signal was locked to a reference voltage using a New Focus LB1005 servo-controller to implement a classical proportional–integral (PI) control system.

Initially, the free-running performance of the QCL was measured to determine the power-drift characteristics and a suitable setpoint for power stabilization. The detector response was demodulated using a 50-ms lock-in time constant, corresponding to a measurement noise of ~140 nV. Figure 5(a) and Fig. 5(c) show the recorded signal and corresponding histogram over a 600-s
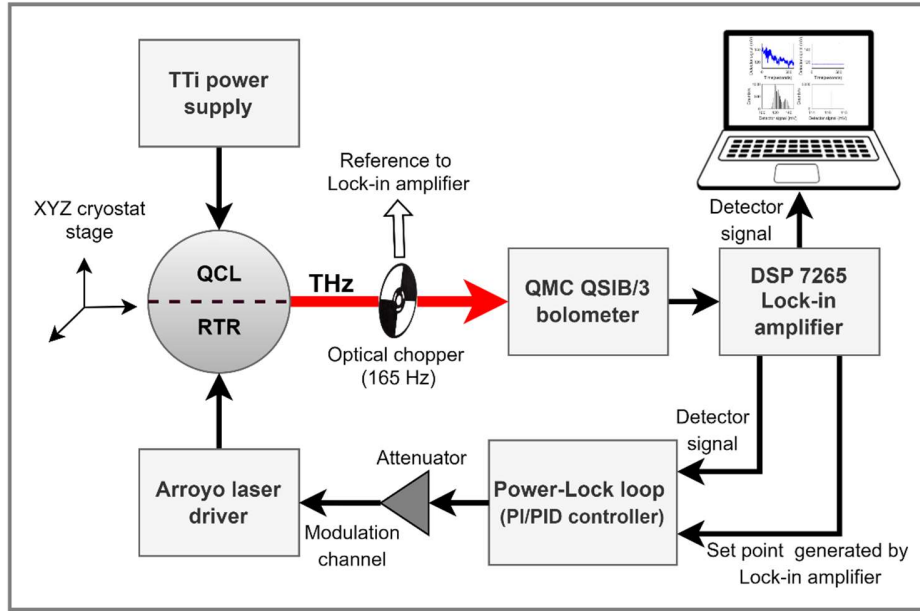
**Fig. 4.** Schematic representation of power-lock system with PI controller.

acquisition time, with a slight beam misalignment introduced used to reduce risk of detector saturation. The measurement shows a bimodal power drift consisting of two metastable points around 122 mV and 135 mV, with full widths at half-maxima of 9.4 mV and 9.1 mV respectively. To suppress this mode-hopping behavior in our power-locking system, we selected a setpoint of 116 mV detector signal, i.e., slightly below the modal power of the lower mode.

Within the power-locking loop, the PI controller generates an error signal $e(t)$, by comparing the demodulated detector signal, $P_{out}(t)$ to the setpoint voltage, $P_{set} = 116$ mV, such that $e(t) = P_{out}(t) - P_{set}$. A control output, $u(t)$, is then generated such that:

$$u(t) = k_p \left[ 1 + \frac{1}{T_i} \int dt \right] e(t) \tag{1}$$

where $k_p$ is the gain coefficient for the proportional-control term, and $T_i$ is the time constant for the integral-control term. These are respectively used to correct for instantaneous deviations and accumulated offsets from the setpoint.

Following the modulation function shown in Fig. 2(b), the QCL output power decreases as the RTR drive-current increases over the range $I_{RTR} = 0$–1 A. To implement this within a control loop, the PI control-signal was connected to the external modulation input on the Arroyo 4302 laser driver using a simple signal-conditioning circuit. This input provides current modulation using an effective transconductance of $g_m = 0.2$ S, over a $V_{mod} = 0$–10 V range. The total time-varying current supplied to the RTR is therefore given by $i_{RTR}(t) = I_0 + 0.2V_{mod}(t)$, where $I_0$ is a quiescent d.c. bias. As such, the control system was designed to operate at a zero-bias point in the middle of the modulator range, and to provide an increase in modulator voltage in response to an increase in the error signal.

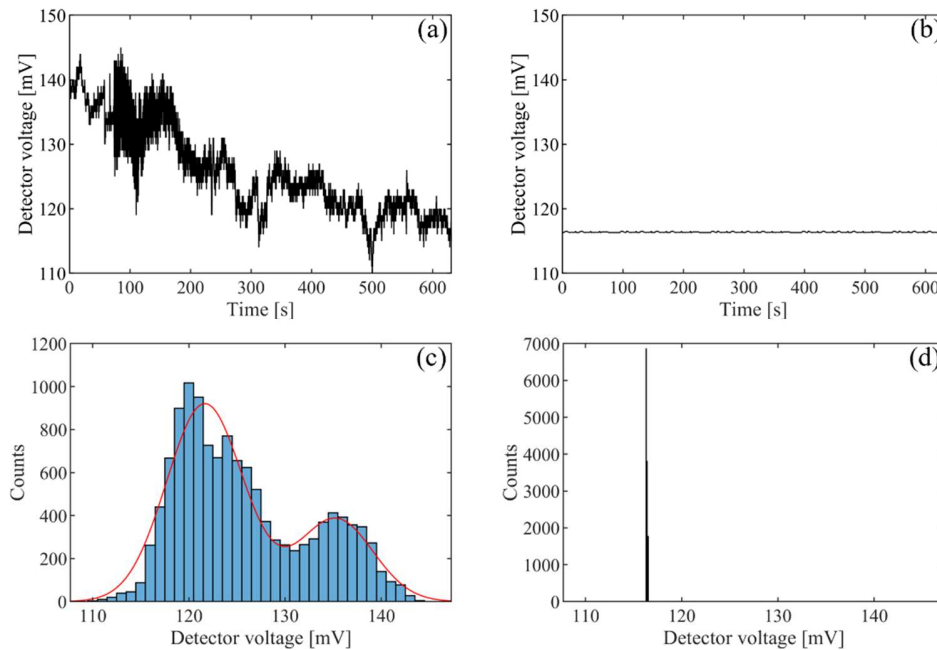$$V_{mod}(t) = \frac{V_{max}}{2} [1 - u(t)] \tag{2}$$

**Fig. 5.** Demodulated time-domain detector signals, using a lock-in time constant of 50 ms for (a) free-running QCL and (b) power-locked QCL. (c),(d) Histograms of the power fluctuations corresponding to the unlocked state and the locked states respectively. The orange curve in (c) is a fitted summation of two Gaussian peaks.

The d.c. bias component was set to $I_0 = 400$ mA to restrict the total modulated current to 300–500 mA to prevent overcurrent damage to the resonator. As a result, the maximum output of the PI controller was limited to 0–10 V and attenuated with a potential divider to 0–1 V.

A standard Ziegler–Nichols approach was used to optimally tune the PI control parameters, resulting in a proportional gain, $k_p = 2$, and integration time $T_i = 0.001$ s. Since the integration time is significantly shorter than the modulation period of the chopper, the integral term of the controller is effectively redundant. As such, the RTR modulator could be used within a simpler proportional control scheme without introducing offset. As a benchmark for THz power-stabilization, we selected the 300-s observation cycle of the "Keystone" (formerly "LOCUS") atmospheric radiometry satellite [18], which was recently selected for a Phase-0 feasibility study in the European Space Agency's Earth Explorer 12 program. Figure 5(b) and (d) show that a mission-compliant power-locking duration was achieved over an arbitrary 623-s measurement, with noise level comparable with the 100 μV resolution of the lock-in amplifier analogue-to-digital convertor.

It is important to note that the RTR current introduces a perturbation to the emission frequency, albeit significantly weaker than that associated with the QCL current. As such, the amplitude stabilization is likely to result in a small increase in frequency fluctuation [6]. A direct time-resolved measurement of this excess frequency noise is challenging, however, and would require either the use of FM–AM conversion, or frequency down-conversion techniques. This effect could be mitigated through a dual-loop control system, in which the QCL current provides a quasi-independent frequency stabilization mechanism.

## 4. Waveguide integration

We have previously demonstrated QCL integration within precision-micromachined metallic waveguide modules at frequencies across the 2–5-THz band [19–22]. This approach has been shown to significantly reduce the far-field beam divergence compared with unmounted double-metal QCLs, provides reproducible mounting, and potentially offers protection against mechanical vibrations and exposure to ionizing radiation. A module design for the integrated RTR-QCL device is shown in Fig. 6(a) and (b), using a split-block approach. A rectangular channel was precision milled into a pair of copper blocks, such that the two halves co-registered to form a hollow rectangular waveguide with dimensions of $(165 \times 82)$ μm$^2$. Each waveguide is coupled into free space using a ~25 dBi diagonal feedhorn. Although the waveguides are overmoded at 3.4-THz, this approach relaxes machining tolerances and has yielded good out-coupling of THz power and a near-Gaussian far-field beam profile in our previous work [19,20]. A recess was milled into the lower half-block, into which the QCL-RTR device was soldered, with each QCL facet coupled into one of the waveguides. Internal and external views of the assembled device are shown in, Fig. 6(c) and (d) respectively.
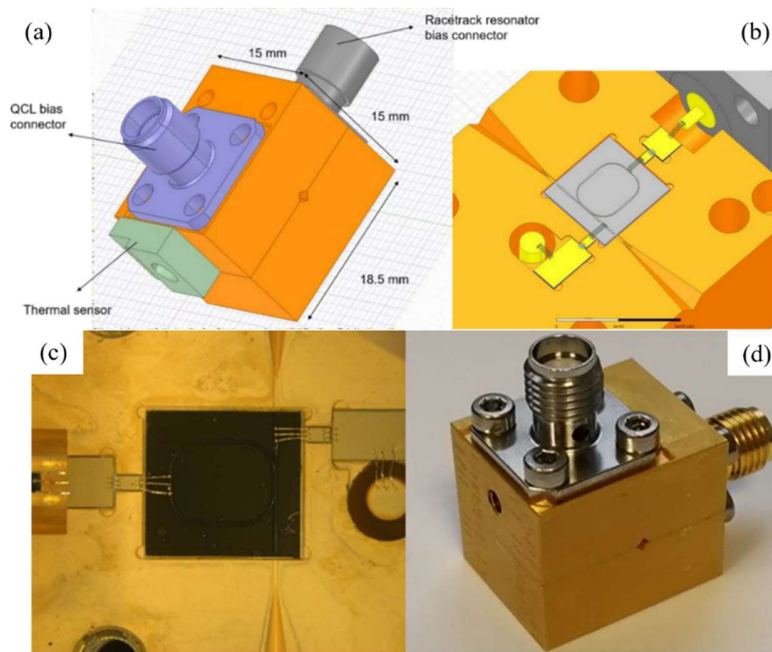


**Fig. 6.** Computer-aided design (CAD) visualizations of (a) the exterior, and (b) the interior lower-half of the QCL–RTR waveguide module. (c) Microscope images of the device integrated into the waveguide assembly, and (d) photograph of an external view of the assembled module.

The module was mounted in a liquid-helium cryostat for characterization as described in Section 2, and an Agilent 8114A pulse generator was used to deliver current pulses to the QCL ridge, with a repetition rate of 10 kHz and a 2% duty cycle. The signal generator provided a 167 Hz square-wave modulation envelope to this electrically gated pulse train, which was used as a reference for lock-in analysis of the bolometric detector signal. The measured light–current–voltage characteristics are shown in Fig. 7. The device operated in pulsed mode up to a maximum operating temperature of 120 K, with a maximum output power at low temperatures of ~70 μW, around 1.3 A. The similar output power, and electrical characteristics to those of

the unmounted case indicate low insertion loss, and low waveguide loss within the module. However, continuous-wave operation was unsuccessful and is likely to be a result of poor thermal performance, as observed in one of our previous recent QCL waveguide-integration studies [21].
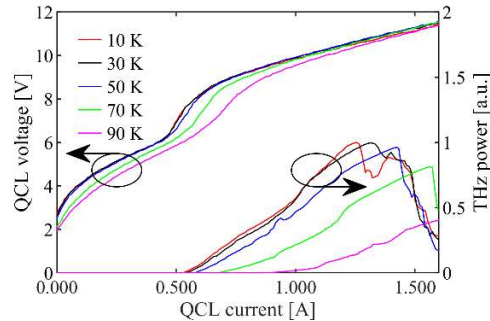


**Fig. 7.** Pulsed light–current–voltage measurements for the waveguide-integrated QCL device. The THz detector signal and QCL terminal voltage are shown as a function of the drive current, with zero bias across the resonator structure.

As continuous-wave operation was not achievable, a power-locking measurement was not feasible. However, the emission and tuning characteristics provide insight into the potential for future such investigations. Figure 8(a) shows the characterization of the emission spectrum of the integrated QCL (in pulsed operation) at different drive current, keeping RTR bias constant at 300 mA. At bias currents above 800 mA, multi-mode emission is observed with a free spectral range (FSR) of ~10 GHz, corresponding to a Fabry–Pérot resonator of length 4 mm (i.e., the length of the QCL ridge). At lower currents, a subset of these modes is observed, indicating that alternate modes are suppressed by the RTR coupling at the middle of the ridge. The multi-mode behavior may be a result of the measurements being undertaken at 10 K compared to the unmounted device at 40 K, which could have increased the gain-bandwidth of the QCL. On the other hand, Fig. 8(b) shows the emission spectrum of the modulator at different RTR drive currents, keeping the QCL bias constant at 720 mA, where only four modes are seen. Under these conditions, the intensity of the principal emission line decreases almost linearly with a modulation coefficient $1.0 \pm 0.2$ $A^{-1}$. This implies that the RTR power modulation effect is approximately three times stronger within the waveguide-integration scheme, compared with the unmounted device. It is possible, therefore, that a cavity enhancement of the modulation
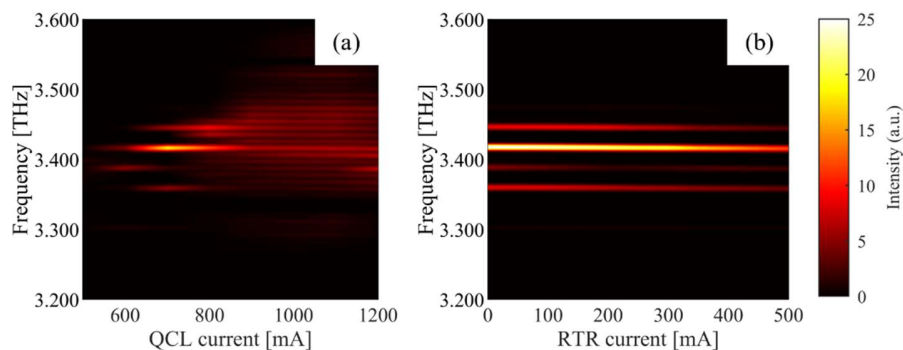


**Fig. 8.** Emission spectra for integrated QCL-RTR device (a) as a function of QCL current, with RTR current constant at 300 mA; (b) as a function of RTR current, with QCL current constant at 720 mA.

occurs. However, it is important to note that this observation is limited to pulsed operation, and multi-mode emission.

## 5. Conclusion

We have successfully demonstrated output power stabilization of a THz QCL using an integrated RTR modulator, within a simple PI control loop. This scheme is potentially advantageous for applications involving satellite deployment, e.g., in support of Earth observation and radio astronomy, as no external THz optical modulator is required and thus enabling compact system design. In the present work, the power locking loop was limited to 20-Hz bandwidth by the relatively slow response time of the bolometric detector, and the need for modulation/demodulation using an optical chopper. Although we have shown that this is fast enough to compensate for thermal drifts observed in a free-running QCL, higher loop bandwidths could potentially be achieved. Indeed, the modulation is implemented through the optoelectronic dynamics of QCL active media, which have previously been shown to enable RF modulation at 35 GHz in single cavities [23], and sub-nanosecond dynamics in coupled cavities [15]. Faster detector technologies, including Schottky-barrier diodes [24], or field-effect-transistors [25,26] could also be used as the power monitor within the system to provide loop bandwidths on the ~GHz scale.

The work presented here supports the development of THz receiver technology targeted for the "Keystone" candidate mission for the ESA Earth Explorer 12 program. As such, further work will focus on integration of QCL-RTR modulators with Schottky-diode mixers, and the development of compact payload packages within space-qualified cryocoolers. The waveguide-module integration results demonstrated here indicate good optical outcoupling and evidence of power modulation. However, thermal, and electromagnetic design improvements will be required to enable continuous-wave, single-mode operation. A further key consideration is the relatively large electrical power consumption of the RTR element, which is comparable to that of the QCL itself. This both increases system power budget requirements and introduces thermal load. The integration approach is, though, attractive in terms of reducing system mass and volume, and the numbers of potential points of failure when compared to the use of external modulators. It may also be possible to engineer alternative active media with tunable intersubband absorption at lower drive currents. Beyond satellite applications, this work underpins further potential applications in modulation schemes for THz communications, or laser stabilization within THz imaging and spectroscopy techniques.

**Disclosures.** The authors declare no conflicts of interest.

**Data availability.** The data associated with this paper are openly available at the University of Leeds repository [27].

## References

1. R. Köhler, A. Tredicucci, F. Beltram, *et al.*, "Terahertz semiconductor-heterostructure laser," Nature **417**(6885), 156–159 (2002).
2. B. Ferguson and X.-C. Zhang, "Materials for terahertz science and technology," Nat. Mater. **1**(1), 26–33 (2002).
3. R. Nelander and A. Wacker, "Temperature dependence of the gain profile for terahertz quantum cascade lasers," Appl. Phys. Lett. **92**(8), 081102 (2008).
4. A. Valavanis, P. Dean, Y. L. Lim, *et al.*, "Self-Mixing Interferometry With Terahertz Quantum Cascade Lasers," IEEE Sens. J. **13**(1), 37–43 (2013).

5. D. M. Slocum, E. J. Slingerland, R. H. Giles, *et al.*, "Atmospheric absorption of terahertz radiation and water vapor continuum effects," J. Quant. Spectrosc. Radiat. Transf. **127**, 49–63 (2013).

6. Y. Ren, D. J. Hayton, J. N. Hovenier, *et al.*, "Frequency and amplitude stabilized terahertz quantum cascade laser as local oscillator," Appl. Phys. Lett. **101**(10), 101111 (2012).

7. B. Wei, S. J. Kindness, N. W. Almond, *et al.*, "Amplitude stabilization and active control of a terahertz quantum cascade laser with a graphene loaded split-ring-resonator array," Appl. Phys. Lett. **112**(20), 201102 (2018).

8. T. Alam, M. Wienold, X. Lü, *et al.*, "Frequency and power stabilization of a terahertz quantum-cascade laser using near-infrared optical excitation," Opt. Express **27**(25), 36846–36854 (2019).

9. M. C. Wanke, E. W. Young, C. D. Nordquist, *et al.*, "Monolithically integrated solid-state terahertz transceivers," Nat. Photonics **4**(8), 565–569 (2010).

10. G. Liang, X. Hu, X. Yu, *et al.*, "Integrated Terahertz Graphene Modulator with 100% Modulation Depth," ACS Photonics **2**(11), 1559–1566 (2015).

11. I. Kundu, P. Dean, A. Valavanis, *et al.*, "Discrete Vernier tuning in terahertz quantum cascade lasers using coupled cavities," Opt. Express **22**(13), 16595–16605 (2014).

12. I. Kundu, P. Dean, A. Valavanis, *et al.*, "Quasi-continuous frequency tunable terahertz quantum cascade lasers with coupled cavity and integrated photonic lattice," Opt. Express **25**, 486–496 (2017).

13. I. Kundu, J. R. Freeman, P. Dean, *et al.*, "Terahertz photonic integrated circuit for frequency tuning and power modulation," Opt. Express **28**(4), 4374–4386 (2020).

14. W. Bogaerts, P. De Heyn, T. Van Vaerenbergh, *et al.*, "Silicon microring resonators," Laser Photonics Rev. **6**(1), 47–73 (2012).

15. I. Kundu, F. Wang, X. Qi, *et al.*, "Ultrafast switch-on dynamics of frequency-tuneable semiconductor lasers," Nat. Commun. **9**(1), 3076 (2018).

16. M. Wienold, L. Schrottke, M. Giehler, *et al.*, "Low-voltage terahertz quantum-cascade lasers based on LO-phonon-assisted interminiband transitions," Electron. Lett. **45**(20), 1030–1031 (2009).

17. S. Barbieri, J. Alton, H. E. Beere, *et al.*, "Heterodyne mixing of two far-infrared quantum cascade lasers by use of a point-contact Schottky diode," Opt. Lett. **29**(14), 1632–1634 (2004).

18. S. P. Rea, B. N. Ellison, B. M. Swinyard, *et al.*, "The Low-Cost Upper-Atmosphere Sounder (LOCUS)," in *26th International Symposium on Space Terahertz Technology* (2015).

19. A. Valavanis, J. X. Zhu, N. Brewster, *et al.*, "Mechanically robust waveguide-integration and beam shaping of terahertz quantum cascade lasers," Electron. Lett. **51**(12), 919–921 (2015).

20. B. N. Ellison, A. Valavanis, O. Auriacombe, *et al.*, "3.5 THz quantum-cascade laser emission from dual diagonal feedhorns," Int. J. Microwave Wireless Technol. **11**(9), 909–917 (2019).

21. E. Nuttall, Y. Han, D. Pardo, *et al.*, "Waveguide integration of a >4.7-THz quantum-cascade laser," Electron. Lett. **59**, e12703 (2023).

22. M. Salih, S. S. Kondawar, N. Brewster, *et al.*, "Integration of a 2.1-THz Quantum Cascade Laser within an IEEE WM-130 Rectangular Metallic Waveguide," in *48th International Conference on Infrared, Millimeter, and Terahertz Waves* (2023), pp. 1–2.

23. P. Gellie, S. Barbieri, J.-F. Lampin, *et al.*, "Injection-locking of terahertz quantum cascade lasers up to 35 GHz using RF amplitude modulation," Opt. Express **18**(20), 20799–20816 (2010).

24. A. Dunn, C. Poyser, P. Dean, *et al.*, "High-speed modulation of a terahertz quantum cascade laser by coherent acoustic phonon pulses," Nat. Commun. **11**, 1–8 (2020).

25. J. Zdanevičius, K. Ikamas, J. Matukas, *et al.*, "TeraFET detector for measuring power fluctuations of 4.75-THz QCL-generated radiation," in *International Conference on Noise and Fluctuations* (2017), pp. 1–4.

26. N. K. North, J. Holstein, M. D. Horbury, *et al.*, "Real-Time Analysis of THz Quantum-Cascade Laser Signals using a Field Effect Transistor Array," in *48th International Conference on Infrared, Millimeter, and Terahertz Waves* (2023), pp. 1–2.

27. S. S. Kondawar, N. K. North, Y. Han, *et al.*, "Data associated with 'Power stabilization of a terahertz-frequency quantum-cascade laser using a photonic-integrated modulator'," University of Leeds (2024), https://dx.doi.org/10.5518/1522.